Extraction of Network Parameters in the Electromagnetic Analysis of Planar Structures Using the Method of Moments

Mostafa N. Abdulla, *Member, IEEE*, and Michael B. Steer, *Fellow, IEEE*

***Abstract*—Integration of electromagnetic (EM) and circuit analyses for the modeling of spatially distributed microwave and millimeter-wave circuits requires the establishment of ports that are defined in both the circuit and EM realms. Four EM techniques are developed here and contrasted for the extraction of the port network parameters at circuit compatible ports. A full-wave method-of-moments EM analysis directly yielding network parameters of a slot–stripline–slot structure is formulated.**

***Index Terms*—Field–circuit interaction, global modeling, Green's functions, method of moments, network characterization.**

I. Introduction

THE method of moments (MoM) is an efficient way of electromagnetically modeling structures as pre-analysis, embedded in the Green's function, is used to reduce the numerical computation that would otherwise be required in more general techniques such as the finite-element method (FEM). This is especially true for antennas and open structures [1]. As subdomain current basis functions and differential (or delta-gap) voltages are used in MoM formulation, the compatibility with general-purpose microwave circuit simulators, which use terminal current and voltage quantities, is near optimum. However, the interface thus defined is not compatible with the simulation of circuits. Several measurement-like electromagnetic (EM) techniques have been presented and shown to be well suited to extracting the scattering or circuit parameters of planar circuits [2]. These are classically deduced from the calculation of the surface current flowing on the structure [3]. This is analogous to slotted-line measurement of a standing-wave pattern and subsequent extraction of a one-port reflection coefficient. Another approach implements a deembedding procedure involving two through lengths of line to compensate for port discontinuities [4], a procedure very similar to that used in actual measurements. This deembedding becomes increasingly complex when parameters at more than two ports are to be extracted, as multiple "measurements" are required [5], [6]. Accuracy is improved by implementing matched terminations in the EM analysis using an integral-equation technique, as in [7] and [8], but more computations of the MoM matrix elements are involved. In the MoM, basis functions of current are used and each, typically a rooftop or half-rooftop function, straddles two geometric cells so that the coefficient of a basis function is the "differential-port" current flowing from one cell into its neighbor. The MoM formulation also uses the voltages between cells as variables, and these are just differential-port voltages if the cells are not electrically connected (i.e., shorted, in which case the voltage is zero). In structures with single-layer metallization, the network parameters so extracted are referenced to the differential ports where active devices are placed and, thus, can be used directly in circuit simulation [9]–[11]. The admittance parameter relationship between the currents and voltages at the differential ports can be extracted from the inverted and reduced form of the MoM matrix (the procedure is described in [12]–[14]).

The situation is more complicated when a ground plane is involved, as inevitably a port is defined with respect to the ground plane. This is because these ports are not differential ports, but are referred to the ground plane (i.e., the voltage is referred to ground). Eleftheriades and Mosig [15] used a half-basis function to define a port at the intersection of the walls of a shielded enclosure. This is an elegant procedure, but not applicable in the absence of an enclosure (in open structures) or ports not at the walls of the enclosure, but inside it. Building on the half-basis function idea, Zhu *et al.*computed external port parameters for unbounded structures [16]. In [16], the authors use a segmentation approach to partition the feed lines from the rest of the circuit. In effect, these feed lines are terminated in a virtual electrical wall and half-basis functions are used. Images of the lines are then used to compute the inner port parameters. However, this approach alters the physical behavior of a circuit in general. Introducing a vertical current element (basis function) in the position of a circuit port is, conceivably, one way of defining the inner circuit port in the MoM formulation. As an example of a more complicated situation, consider the problem of defining circuit ports for the extraction of the network parameters of a large open planar structure such as the slot–stripline–slot (SSS) spatial power combining amplifier shown in Fig. 1 [17], [18]. Each dimension of this system is around two wavelengths and

Manuscript received July 14, 1999. This work was supported by the U.S. Army Research Office through Clemson University as a Multidisciplinary University Research Initiative on Quasi-Optical Power Combining under Agreement DAAG55-97-K-0132.

M. N. Abdulla is with the Intel Corporation, Sacramento, CA 95827-3500 USA (e-mail: mnabdull@ieee.org).

M. B. Steer is with the Electrical and Computer Engineering Department, North Carolina State University, Raleigh, NC 27695-7914 USA (e-mail: m.b.steer@ieee.org).

Publisher Item Identifier S 0018-9480(01)00023-0.

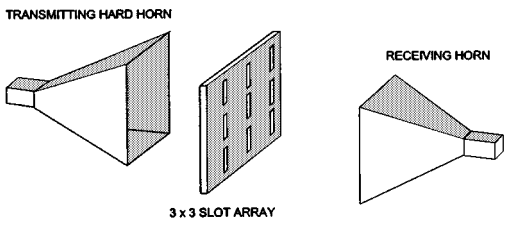

Fig. 1. SSS spatial power-combining system showing a simplified 3×3 array.

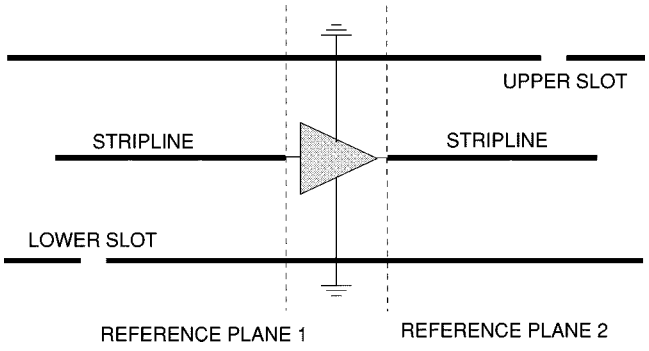

Fig. 2. SSS amplifier unit cell.

is arranged as an $N \times N$ array of unit amplifiers. Each unit cell of the array is composed of an input stripline-coupled slot antenna, then a stripline-mounted monolithic-microwave integrated-circuit (MMIC) amplifier, and finally, an output antenna (see Fig. 2).

The tight coupling of the antenna, circuit, and EM environments requires global modeling of the entire finite-sized structure and strategies for treating the EM model as an integral part of the circuit model [14], [19], [20].

The aim of the overall analysis is to develop a single network representation of the EM structure. The network is interfaced to circuit models at "EM terminals" defined to be consistent with nodal-based circuit descriptions. The depiction shown in Fig. 3 shows how the passive structure is reduced to an integrated model for a unit cell. In modeling an $N \times N$ array, the two-port network is replaced by a network with $2N^2$ ports and the input excitation is modeled using N equivalent sources at the input-side ports of the network. Each of the ports in Fig. 3 must be interfaced to the conventional circuit at normal current/voltage-defined terminals referenced to the ground planes. The terminals so referenced are called "circuit ports," whereas the ports immediately available from MoM analysis are differential ports [10], [11], [14]. The main contribution of this paper is the development and contrasting of a number of techniques for extracting the immittance parameters at circuit ports from the EM characterization at differential ports. Earlier work by our group relates these to the nodal parameters required by circuit simulators [9], [20]. A mixed-potential integral equation (MPIE), implementing the ideas developed here, is also developed for the full-wave analysis of the SSS structure shown in Figs. 3 and 4 accounting for an incident EM field at the slot array.

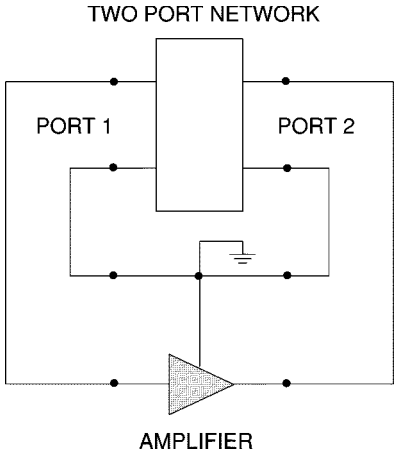

Fig. 3. SSS unit cell equivalent network.

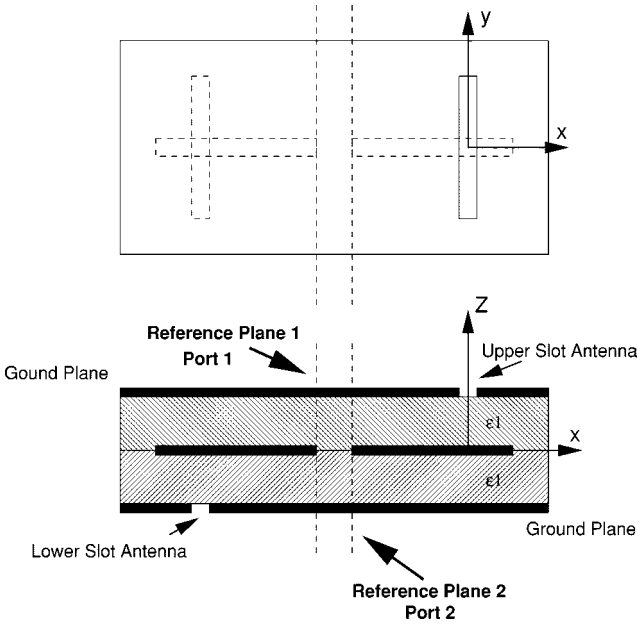

Fig. 4. SSS unit cell.

II. Network Characterization

Without loss of generality, consider the structure in Fig. 4. Circuit compatibility requires that the parameters be referred to ports, each of which has one terminal located on the stripline and the other located at the ground plane (assuming that the two ground planes are electrically identical). However, only differential ports, with each port having two terminals located on either side of a break in the stripline, are immediately available from EM analysis. In this section, the four techniques illustrated in Fig. 5 are considered for translating the parameters extracted at the differential ports to parameters referred to the circuit ports. The first, i.e., Fig. 5(a), uses standard *standing-wave characterization* determined by detecting the standing-wave pattern on the line. This is practically used only for characterizing one port at a time and multiport characterization obtained using various impedance terminations at ports not being driven. However only one MoM matrix fill operation

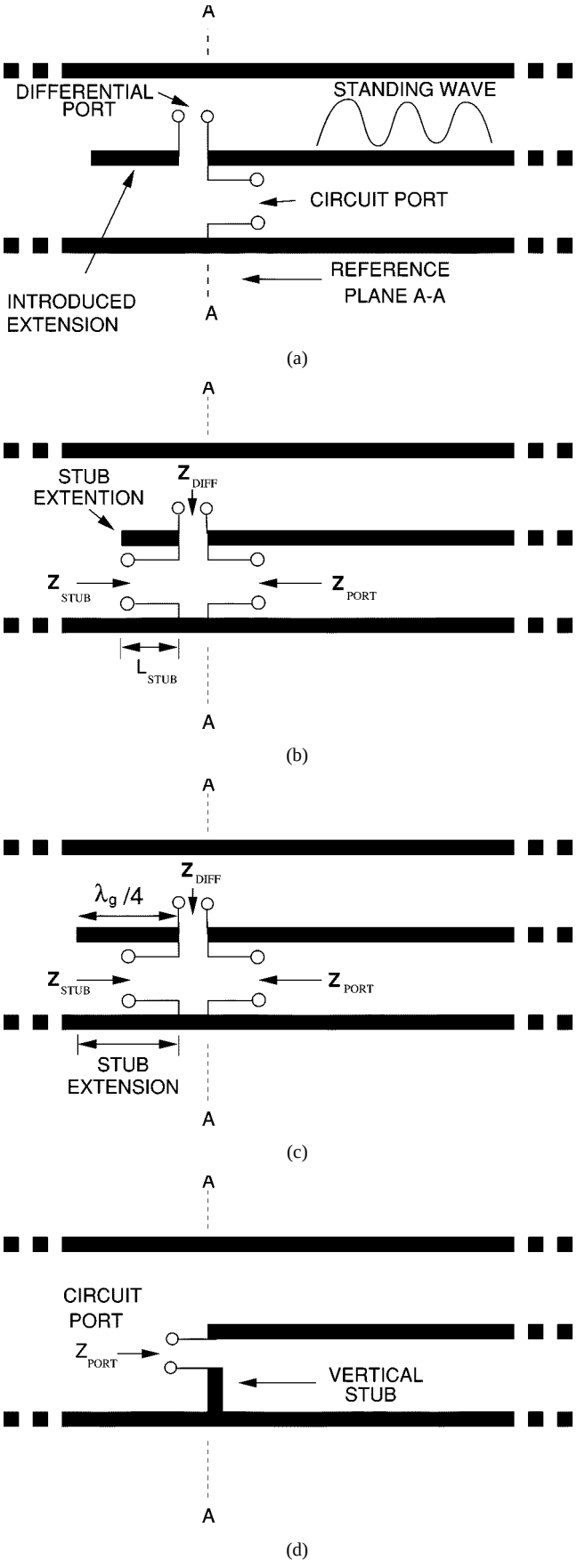

Fig. 5. Four techniques for establishing a circuit ports in MoM analysis. (a) Standing-wave characterization. (b) Stub deembedding. (c) Quarter-wavelength stub. (d) Vertical stub.

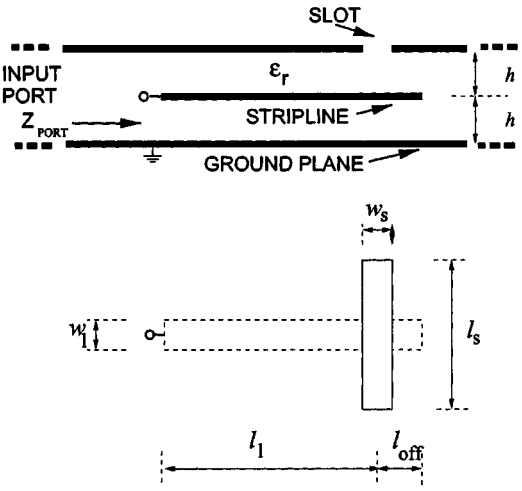

Fig. 6. Single port.

is required. The *stub deembedding* technique, i.e., Fig. 5(b), is also used for one-port characterization, subsequently removing the impedance of the open-circuit stub from the differential impedance to obtain the circuit port impedance. The third approach, i.e., Fig. 5(c), uses an open circuit *quarter-wavelength stub* to present a short circuit at one terminal of a differential port—thus transforming the differential port into the desired circuit port. In the final technique, i.e., Fig. 5(d), a *vertical stub* effectively introduces a conductor from the ground plane to the stripline so that the differential port between the wire and stripline becomes the desired circuit port in the MoM formulation. The techniques are described in greater detail below in reference to the extraction of the input impedance $Z_{\rm PORT}$ of the simpler structure in Fig. 6.

A. Standing-Wave Characterization

The *standing-wave characterization* method mimics a laboratory measurement procedure as a source is applied to a port and the standing-wave pattern detected [see Fig. 5(a)]. Here, a delta-gap source is introduced between two MoM cells at the differential port. The standing-wave pattern enables the input reflection coefficient to be determined and referred to the desired reference plane. In this manner, the discontinuity introduced by the source and line extension do not affect the characterization. Multiport parameters are obtained by either exciting one port at a time and detecting the standing-wave pattern at the other port, or by determining the input reflection coefficient at one port at a time with various loads at the other ports using a multiport extraction procedure [5], [6]. The number of permutations increases combinatorially as the number of ports increases. Generally, an additional length of the line, at least one wavelength long, must be introduced between the excitation source and the reference plane to ensure TEM propagation where the standing-wave pattern is detected. However, in some situations, it may not be possible to insert such a long line because of the presence of other structures or the introduction of EM effects that were not present in the original structure. Fortunately, if the line can be inserted without interfering with the structure being model, coupling between the added line and the rest of the circuit can be excluded during matrix fill. A further problem with

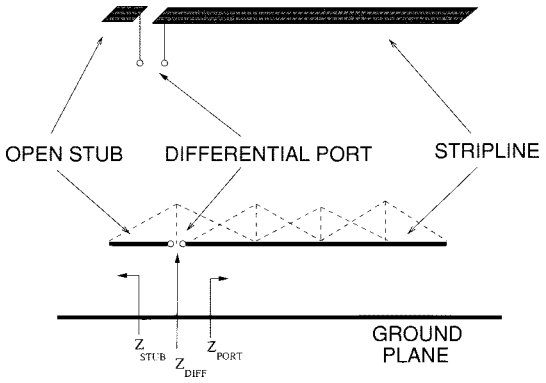

Fig. 7. Port definition for differential port and the differential bases cells.

this method is that the characteristic impedance of the open stub must be determined separately.

B. Stub Deembedding

The stub deembedding procedure is illustrated in Fig. 5(b). The input impedance calculated directly from MoM is the impedance $Z_{\rm DIFF}$ looking into the differential port, which is the series combination of $Z_{\rm PORT}$ and the stub impedance $Z_{\rm STUB}$ (see Fig. 7) so that

$$Z_{\rm PORT} = Z_{\rm DIFF} - Z_{\rm STUB} \tag{1}$$

$Z_{\rm STUB} = Z_c \coth(\gamma L_{\rm STUB})$ where the characteristic impedance Z_c and the propagation constant γ can be determined analytically or numerically.

For an N-port structure, an $N \times N$ differential impedance matrix $\mathbf{Z}_{\rm DIFF}$ can be extracted from the inverted and then reduced form of the MoM impedance matrix (the method is detailed in [14]). The $\mathbf{Z}_{\rm PORT}$ matrix, also $N \times N$, is then

$$\mathbf{Z}_{\rm PORT} = \mathbf{Z}_{\rm DIFF} - \mathbf{Z}_{\rm STUB} \tag{2}$$

and $\mathbf{Z}_{\rm STUB}$ is a diagonal matrix with elements $Z_{{\rm STUB},i}$, $i = 1, \ldots, N$ at the ith port. This method is computationally efficient, as there is only one MoM matrix fill and solve. However, the method neither accounts for fringing effects at the end of the stub, nor possible non-TEM mode excitation on the stub, and it increases the size of the MoM matrix. Also, as with the two-port structure in Fig. 4, it is not always physically possible to insert the stub, even if it is of the minimum half-basis function length.

C. Quarter-Wavelength Stub

If the stub of the previous technique is one quarter-wavelength long, as in Fig. 5(c), $\mathbf{Z}_{\rm PORT}$ can be calculated directly from the MoM as then $\mathbf{Z}_{\rm STUB} = \mathbf{0}$ and thus $\mathbf{Z}_{\rm PORT} = \mathbf{Z}_{\rm DIFF}$. The open-circuit stub increases the MoM matrix size and has the same drawbacks as the previous method, but has the advantage that the characteristic impedance of the stub is not required. Note that the physical length of the stub must be changed with frequency. This approach is similar to that of Zhu *et al.* [16] who use images in a ground wall to create a short circuit.

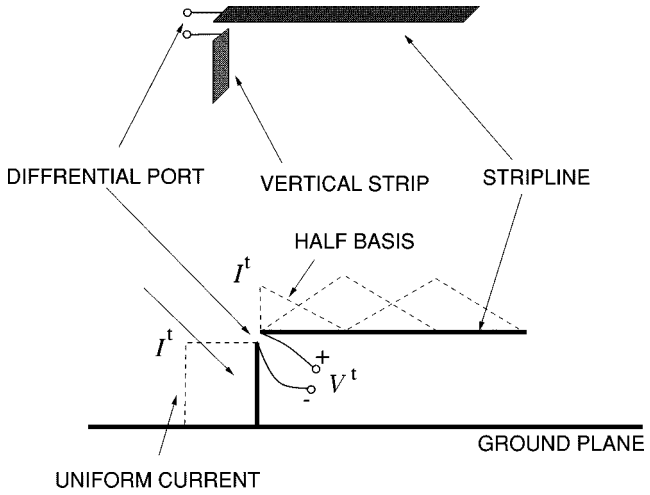

Fig. 8. Port definition for a unit cell using vertical current cell and half-cell.

D. Vertical Stub

The introduction of a vertical stub, as in Fig. 5(d), brings the ground reference up to the strip and forms a differential port, which approximates the circuit port $\mathbf{Z}_{\rm PORT} \approx \mathbf{Z}_{\rm DIFF}$. Appropriate basis function selections for one port are shown in Fig. 8. That is, a half-rooftop basis function on the strip side of the port and a pulse basis function on the vertical stub, both with current I^t, at the port terminals. The constraint imposed by I^t being the coefficient of two basis functions results in an expanded form of the MoM impedance matrix for an N-port system

$$\begin{bmatrix} \mathbf{Z}^{cc} & \mathbf{Z}^{ct} \\ \mathbf{Z}^{tc} & \mathbf{Z}^{tt} \end{bmatrix} \begin{bmatrix} \mathbf{I}^c \\ \mathbf{I}^t \end{bmatrix} = \begin{bmatrix} \mathbf{0} \\ \mathbf{V}^t \end{bmatrix} \tag{3}$$

where the superscript t denotes terminal quantities and the superscript c denotes quantities pertinent to currents induced on the conductor surface. I^c and I^t are the vectors of conductor and terminal current, respectively. $\mathbf{Z}^{cc}$ in (3) is the MoM impedance matrix using the full rooftop basis functions. $\mathbf{V}^t$ is the vector of delta-gap voltage generators at the circuit ports and $\mathbf{I}^t$ is the vector of the port currents. The port admittance matrix $\mathbf{Y}^t$ (defined by $\mathbf{I}^t = \mathbf{Y}^t\mathbf{V}^t$) is obtained as follows. From (3)

$$\begin{bmatrix} \mathbf{I}^c \\ \mathbf{I}^t \end{bmatrix} = \begin{bmatrix} \mathbf{Z}^{cc} & \mathbf{Z}^{ct} \\ \mathbf{Z}^{tc} & \mathbf{Z}^{tt} \end{bmatrix}^{-1} \begin{bmatrix} \mathbf{0} \\ \mathbf{V}^t \end{bmatrix} \tag{4}$$

or

$$\begin{bmatrix} \mathbf{I}^c \\ \mathbf{I}^t \end{bmatrix} = \begin{bmatrix} \mathbf{Y}^{cc} & \mathbf{Y}^{ct} \\ \mathbf{Y}^{tc} & \mathbf{Y}^{tt} \end{bmatrix} \begin{bmatrix} \mathbf{0} \\ \mathbf{V}^t \end{bmatrix}. \tag{5}$$

Then, $\mathbf{Y}^t = \mathbf{Y}^{tt}$ (5), which is the $N \times N$ submatrix in the lower right-hand corner of the inverted impedance matrix in (4). This method introduces the smallest discontinuity and can be used with any multiport configuration in microstrip or stripline.

III. Structure Geometry and Modeling

The EM modeling of the SSS structure in Fig. 4 begins with the development of the Green's functions following the approach in [21] and using the MPIE and MoM techniques presented in [22] and [23]. First, using the equivalence principle

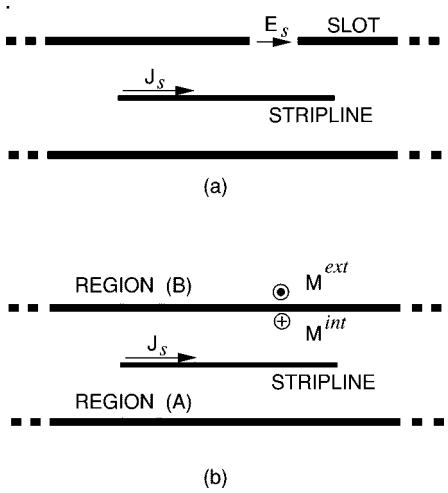

Fig. 9. Single SSS cell. (a) Original structure. (b) Structure after application of the equivalence principle.

[24], the center conductor at $z = 0$ in Fig. 4 is removed and replaced by an equivalent electric surface current density J_s. The slot, at the $z = h$ plane, is then removed and replaced by perfect electric conductors, and the equivalent magnetic surface current density flowing at $z = h^-$ is

$$\mathbf{M}_s^{\text{int}} = \hat{z} \times \mathbf{E}_s. \tag{6}$$

Finally, for the fields in region $z > h$, the equivalent source is a magnetic surface current density flowing at $z > h^+$ and given by

$$\mathbf{M}_s^{\text{ext}} = -\mathbf{M}_s^{\text{int}}. \tag{7}$$

Thus, the structure is decomposed into two regions, as shown in Fig. 9, and the analysis reduces to determining the induced electric and magnetic surface current densities $\mathbf{J}_s$ and $\mathbf{M}_s^{\text{int}}$. This is accomplished using MoM formulation, which solves the MPIEs whose kernels are the Green's functions.

IV. MPIEs

In the internal region, i.e., region A in Fig. 9(b), the electric- and magnetic-field distributions can be expressed as

$$\mathbf{E}^{\text{int}}(\mathbf{r}) = \mathbf{E}_{\text{inc}}^{\text{int}}(\mathbf{r}) - j\omega\mathbf{A}^{\text{int}}(\mathbf{r}) - \nabla\phi^{\text{int}}(\mathbf{r}) - \frac{1}{\epsilon}\nabla \times \mathbf{F}^{\text{int}}(\mathbf{r}) \tag{8}$$

$$\mathbf{H}^{\text{int}}(\mathbf{r}) = \mathbf{H}_{\text{inc}}^{\text{int}}(\mathbf{r}) - j\omega\mathbf{F}^{\text{int}}(\mathbf{r}) - \nabla\psi^{\text{int}}(\mathbf{r}) + \frac{1}{\mu_0}\nabla \times \mathbf{A}^{\text{int}}(\mathbf{r}) \tag{9}$$

where $\mathbf{E}_{\text{inc}}^{\text{int}}(\mathbf{r})$ and $\mathbf{H}_{\text{inc}}^{\text{int}}(\mathbf{r})$ are the incident fields from the external excitation at the slots. $\mathbf{A}^{\text{int}}(\mathbf{r})$, $\mathbf{F}^{\text{int}}(\mathbf{r})$, $\phi^{\text{int}}(\mathbf{r})$, and $\psi^{\text{int}}(\mathbf{r})$ are the vector and scalar potentials of the electric and magnetic sources, respectively. In the external regions, regions B and C in Fig. 9(b), there are no electric sources; thus, the electric- and magnetic-field distributions can be expressed as

$$\mathbf{E}^{\text{ext}}(\mathbf{r}) = \mathbf{E}_{\text{inc}}^{\text{ext}}(\mathbf{r}) - \frac{1}{\epsilon_0}\nabla \times \mathbf{F}^{\text{ext}}(\mathbf{r}) \tag{10}$$

$$\mathbf{H}^{\text{ext}}(\mathbf{r}) = \mathbf{H}_{\text{inc}}^{\text{ext}}(\mathbf{r}) - j\omega\mathbf{F}^{\text{ext}}(\mathbf{r}) - \nabla\psi^{\text{ext}}(\mathbf{r}). \tag{11}$$

Hence, $\mathbf{E}_{\text{inc}}^{\text{ext}}(\mathbf{r})$ and $\mathbf{H}_{\text{inc}}^{\text{ext}}(\mathbf{r})$ are the field distributions of the incident waves from the external regions (B and C). $\mathbf{F}^{\text{ext}}(\mathbf{r})$ and $\psi^{\text{ext}}(\mathbf{r})$ are the vector and scalar potentials of the magnetic sources, which are located immediately above the upper ground plane. Once the electric- and magnetic-field distributions are defined, the boundary conditions are enforced at both the stripline and aperture. Since the tangential components of the electric field are zero on the stripline, the boundary condition is formulated as

$$\mathbf{E}^{\text{int}}(\mathbf{r}) = 0|_{\text{STRIPLINE}}. \tag{12}$$

The tangential components of the magnetic fields are also continuous across the aperture so that

$$\mathbf{H}^{\text{int}}(\mathbf{r}) = \mathbf{H}^{\text{ext}}(\mathbf{r})|_{\text{APERTURE}}. \tag{13}$$

V. Green's Functions

The potentials of the electric and magnetic sources $\mathbf{A}^{\text{int}}(\mathbf{r})$, $\mathbf{F}^{\text{int}}(\mathbf{r})$, $\mathbf{F}^{\text{ext}}(\mathbf{r})$, $\phi^{\text{int}}(\mathbf{r})$, $\psi^{\text{int}}(\mathbf{r})$, and $\psi^{\text{ext}}(\mathbf{r})$ can be represented as

$$\mathbf{A}^{\text{int}}(\mathbf{r}) = \int_{S_1} \bar{\bar{\mathbf{G}}}_A^{\text{int}}(\mathbf{r}, \mathbf{r}') \cdot \mathbf{J}_s(\mathbf{r}')\, dS_1' \tag{14}$$

$$\phi^{\text{int}}(\mathbf{r}) = \int_{S_1} G_\phi^{\text{int}}(\mathbf{r}, \mathbf{r}')\rho_s(\mathbf{r}')\, dS_1' \tag{15}$$

$$\mathbf{F}^{\text{int}}(\mathbf{r}) = \int_{S_2} \bar{\bar{\mathbf{G}}}_F^{\text{int}}(\mathbf{r}, \mathbf{r}') \cdot \mathbf{M}_s(\mathbf{r}')\, dS_2' \tag{16}$$

$$\psi^{\text{int}}(\mathbf{r}) = \int_{S_2} G_\psi^{\text{int}}(\mathbf{r}, \mathbf{r}')\rho_{m_s}(\mathbf{r}')\, dS_2' \tag{17}$$

$$\mathbf{F}^{\text{ext}}(\mathbf{r}) = \int_{S_2} \bar{\bar{\mathbf{G}}}_F^{\text{ext}}(\mathbf{r}, \mathbf{r}') \cdot \left[-\mathbf{M}_s(\mathbf{r}')\right] dS_2' \tag{18}$$

$$\psi^{\text{ext}}(\mathbf{r}) = \int_{S_2} G_\psi^{\text{ext}}(\mathbf{r}, \mathbf{r}')\left[-\rho_{m_s}(\mathbf{r}')\right] dS_2'. \tag{19}$$

where $\bar{\bar{\mathbf{G}}}_A^{\text{int}}(\mathbf{r}, \mathbf{r}')$, $\bar{\bar{\mathbf{G}}}_F^{\text{int}}(\mathbf{r}, \mathbf{r}')$, and $\bar{\bar{\mathbf{G}}}_F^{\text{ext}}(\mathbf{r}, \mathbf{r}')$ are the spatial-domain dyadic Green's functions of vector potentials from the electric and magnetic currents in the internal and external regions (see the Appendix). $G_\phi^{\text{int}}(\mathbf{r}, \mathbf{r}')$, $G_\psi^{\text{int}}(\mathbf{r}, \mathbf{r}')$, and $G_\psi^{\text{ext}}(\mathbf{r}, \mathbf{r}')$ are the spatial-domain Green's functions of scalar potentials from the electric and magnetic charges in the internal and external regions, respectively (see the Appendix). S_1 and S_2 represent the stripline and aperture surfaces, respectively. The quantities $\rho_s(\mathbf{r}')$ and $\rho_{m_s}(\mathbf{r}')$ are electric and magnetic charges, and they are related to $\mathbf{J}_s(\mathbf{r}')$ and $\mathbf{M}_s(\mathbf{r}')$ by the continuity equations

$$\nabla.\mathbf{J}_s = -j\omega\rho_s \tag{20}$$

$$\nabla.\mathbf{M}_s = -j\omega\rho_{m_s}. \tag{21}$$

VI. MoM

The MoM formulation is developed by expanding and testing the MPIE using Galerkin's method to form a linear system of equations, which is the MoM matrix set of equations. Assuming

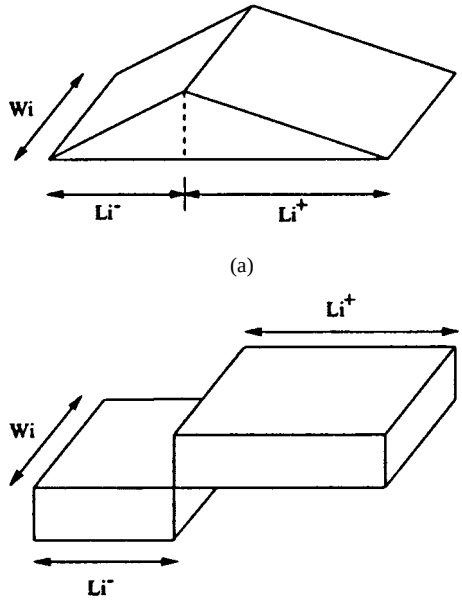

Fig. 10. Basis function. (a) Rooftop. (b) Pulse doublet.

that the electric current density $\mathbf{J}_s$ flows in the x-direction and the magnetic current density $\mathbf{M}_s$ flows in the y-direction, then the electric and magnetic currents densities are expanded as

$$\mathbf{J}_s(\mathbf{r}) = \sum_{n=1}^{N} I_n T_n^x(\mathbf{r}) \tag{22}$$

$$\mathbf{M}_s(\mathbf{r}) = \sum_{m=1}^{M} V_m T_m^y(\mathbf{r}). \tag{23}$$

where T_n^x and T_m^y are rooftop basis functions, as shown in Fig. 10(a). They are defined by

$$T_i^s(s) = \begin{cases} \dfrac{1+(s-s_i)/L_i}{W_i}, & s_i - L_i < s < s_i \\ \dfrac{1-(s-s_i)/L_i}{W_i}, & s_i < s < s_i + L_i \\ 0, & \text{otherwise} \end{cases} \tag{24}$$

where $s = x$ or y. The surface charge density is found using the continuity equation, resulting in pulse doublets [see Fig. 10(b)]

$$\Pi_i^s(s) = \begin{cases} \dfrac{-1}{L_i W_i}, & s_i - L_i < s < s_i \\ \dfrac{1}{L_i W_i}, & s_i < s < s_i + L_i \\ 0, & \text{otherwise} \end{cases} \tag{25}$$

where, again, $s = x$ or y. Upon introducing these distribution functions into the MPIEs and testing them with T_k^x, $k = 1$ to N, and T_l^y, $l = 1$ to M, the following system of integral equations is obtained:

$$\begin{aligned} \left\langle \mathbf{E}_{\text{inc}}^{\text{int}}, T_k^x \right\rangle = {} & j\omega \left\langle \mathbf{A}_t^{\text{int}}, \mathbf{T}_k \right\rangle + \left\langle (\nabla\phi^{\text{int}})_t, T_k^x \right\rangle \\ & + \frac{1}{\epsilon} \left\langle (\nabla \times \mathbf{F}^{\text{int}})_t, T_k^x \right\rangle, \\ & k = 1 \text{ to } N \end{aligned} \tag{26}$$

$$\begin{aligned} \left\langle (\mathbf{H}_{\text{inc}}^{\text{int}} - \mathbf{H}_{\text{inc}}^{\text{ext}})_t, T_l^y \right\rangle = {} & j\omega \left\langle (\mathbf{F}^{\text{int}} - \mathbf{F}^{\text{ext}})_t, T_l^y \right\rangle \\ & + \left\langle (\nabla\psi^{\text{int}} - \nabla\psi^{\text{int}})_t, T_l^y \right\rangle \\ & - \frac{1}{\mu_0} \left\langle (\nabla \times \mathbf{A}^{\text{int}})_t, T_l^y \right\rangle, \\ & l = 1 \text{ to } M \end{aligned} \tag{27}$$

where $\langle , \rangle$ specifies the inner product operation and the subscript t refers to the tangential components in the x–y-plane. After reformulating the integral equations above, the matrix equation

$$\begin{bmatrix} \langle \Delta H^{\text{inc}}, T_l^y \rangle \\ \langle E_s^{\text{inc}}, T_k^x \rangle \end{bmatrix} = \begin{bmatrix} \mathbf{Y} & \mathbf{U} \\ \mathbf{W} & \mathbf{Z} \end{bmatrix} \begin{bmatrix} \mathbf{V} \\ \mathbf{I} \end{bmatrix} \tag{28}$$

is obtained. $\mathbf{Y}_{M\times M}$ is the self-coupling submatrix of the slot, $\mathbf{Z}_{N\times N}$ is the self-coupling submatrices of the stripline, $\mathbf{U}_{M\times N}$ is the coupling submatrix between the slot and the stripline, ; and $\mathbf{W}_{N\times M}$ is the coupling submatrix between the stripline and slot. The vectors $\mathbf{V}_{M\times 1}$ and $\mathbf{I}_{N\times 1}$ are the unknown coefficients of the basis functions on the slot and stripline, respectively. Finally, this matrix is composed of submatrices, with each describing the interaction of two regions of the equivalent model in Fig. 9(b). $[\langle \Delta H^{\text{inc}}, T_l^y \rangle]_{M\times 1}$, $[\langle E^{\text{inc}}, T_k^x \rangle]_{N\times 1}$ are the excitation vectors from the incident fields.

The MoM matrix in (28) is further partitioned two ways: an internal region matrix and an external region matrix. Here, the Green's functions of the external and internal regions are calculated separately, and they depend on the cascading structures [25]. The matrix in (28) is, therefore, calculated as

$$\begin{bmatrix} \mathbf{Y} & \mathbf{U} \\ \mathbf{W} & \mathbf{Z} \end{bmatrix} = \begin{bmatrix} \mathbf{Y}^{\text{ext}} & \mathbf{0} \\ \mathbf{0} & \mathbf{0} \end{bmatrix} + \begin{bmatrix} \mathbf{Y}^{\text{int}} & \mathbf{U}^{\text{int}} \\ \mathbf{W}^{\text{int}} & \mathbf{Z}^{\text{int}} \end{bmatrix} \tag{29}$$

where $\mathbf{Y}^{\text{ext}}$ is the mutual coupling integrals for the external region and $\mathbf{Y}^{\text{int}}$, $\mathbf{U}^{\text{int}}$, $\mathbf{W}^{\text{int}}$, and $\mathbf{Z}^{\text{int}}$ are the mutual coupling for the closed-array structure with ji elements

$$\begin{aligned} Z_{ji}^{\text{int}} = {} & j\omega \left\langle (\mathbf{A}_{ji}^{\text{int}})_t, T_j^x \right\rangle + \left\langle (\nabla\phi_{ji}^{\text{int}})_t, T_j^x \right\rangle \\ = {} & j\omega \int_{y_j-(W_j/2)}^{y_j+(W_j/2)} \int_{x_j-L_j}^{x_j+L_j} \int_{y_i-(W_i/2)}^{y_i+(W_i/2)} \int_{x_i-L_i}^{x_i+L_i} \\ & \cdot T_j^x(x) G_{A_{xx}}^{\text{int}}(x|x'; y|y'; 0|0) T_i^x(x')\, dx'\, dy'\, dx\, dy \\ & - \frac{1}{j\omega} \int_{y_j-(W_j/2)}^{y_j+(W_j/2)} \int_{x_j-L_j}^{x_j+L_j} \int_{y_i-(W_i/2)}^{y_i+(W_i/2)} \int_{x_i-L_i}^{x_i+L_i} \\ & \cdot \Pi_j^x(x) G_{\phi}^{\text{int}}(x|x'; y|y'; 0|0) \Pi_i^x(x')\, dx'\, dy'\, dx\, dy \end{aligned} \tag{30}$$

$$\begin{aligned} Y_{ji}^{\text{int}} = {} & j\omega \left\langle (\mathbf{F}_{ji}^{\text{int}})_t, T_j^y \right\rangle + \left\langle (\nabla\psi_{ji}^{\text{int}})_t, T_j^y \right\rangle \\ = {} & j\omega \int_{x_j-(W_j/2)}^{x_j+(W_j/2)} \int_{y_j-(W_i/2)-L_j}^{y_j+L_j} \int_{x_i-(W_i/2)}^{x_i+(W_i/2)} \int_{y_i-L_i}^{y_i+L_i} \\ & \cdot T_j^y(y) G_{F_{yy}}^{\text{int}}(x|x'; y|y'; h|h) T_i^y(y')\, dx'\, dy'\, dx\, dy \\ & - \frac{1}{j\omega} \int_{x_j-(W_j/2)}^{x_j+(W_j/2)} \int_{y_j-L_j}^{y_j+L_j} \int_{x_i-(W_i/2)}^{x_i+(W_i/2)} \int_{y_i-L_i}^{y_i+L_i} \\ & \cdot \Pi_j^y(y) G_{\psi}^{\text{int}}(x|x'; y|y'; h|h) \Pi_i^y(y')\, dx'\, dy'\, dx\, dy \end{aligned} \tag{31}$$

$$
\begin{aligned}
Y_{ji}^{\text{ext}} &= j\omega\left\langle (\mathbf{F}_{ji}^{\text{ext}})_t,\, T_j^y\right\rangle + \left\langle (\nabla\psi_{ji}^{\text{ext}})_t,\, T_j^y\right\rangle \\
&= j\omega \int_{x_j-(W_j/2)}^{x_j+(W_j/2)} \int_{y_j-L_j}^{y_j+L_j} \int_{x_i-(W_i/2)}^{x_i+(W_i/2)} \int_{y_i-L_i}^{y_i+L_i} \\
&\quad \cdot T_j^y(y) G_{F_{yy}}^{\text{ext}}(x|x';\, y|y';\, h|h) T_i^y(y')\, dx'\, dy'\, dx\, dy \\
&\quad - \frac{1}{j\omega} \int_{x_j-(W_j/2)}^{x_j+(W_j/2)} \int_{y_j-L_j}^{y_j+L_j} \int_{x_i-(W_i/2)}^{x_i+(W_i/2)} \int_{y_i-L_i}^{y_i+L_i} \\
&\quad \cdot \Pi_j^y(y) G_{\psi}^{\text{ext}}(x|x';\, y|y';\, h|h) \Pi_i^y(y')\, dx'\, dy'\, dx\, dy
\end{aligned} \tag{32}
$$

$$
\begin{aligned}
W_{ji}^{\text{int}} &= \frac{1}{\epsilon}\left\langle (\nabla\times\mathbf{F}_{ji}^{\text{int}})_t,\, T_j^x\right\rangle \\
&= \frac{1}{\epsilon} \int_{x_j-(W_j/2)}^{x_j+(W_j/2)} \int_{y_j-L_j}^{y_j+L_j} \int_{y_i-(W_i/2)}^{y_i+(W_i/2)} \int_{x_i-L_i}^{x_i+L_i} \\
&\quad \cdot T_j^y(x) \left[\frac{\partial}{\partial z} G_{F_{yy}}^{\text{int}}(r|r')\right]\Bigg|_{z=0,\, z'=h} T_i^x(y') \\
&\quad \cdot\, dx'\, dy'\, dx\, dy
\end{aligned} \tag{33}
$$

$$
\begin{aligned}
U_{ji}^{\text{int}} &= -\frac{1}{\mu_0}\left\langle (\nabla\times\mathbf{A}_{ji}^{\text{int}})_t,\, T_j^y\right\rangle \\
&= -\frac{1}{\mu_0} \int_{y_j-(W_j/2)}^{y_j+(W_j/2)} \int_{x_j-L_j}^{x_j+L_j} \int_{x_i-(W_i/2)}^{x_i+(W_i/2)} \int_{y_i-L_i}^{y_i+L_i} \\
&\quad \cdot T_j^x(x) \left[\frac{\partial}{\partial z} G_{A_{xx}}^{\text{int}}(r|r')\right]\Bigg|_{z=h,\, z'=0} T_i^y(y') \\
&\quad \cdot\, dx'\, dy'\, dx\, dy.
\end{aligned} \tag{34}
$$

With the vertical stub, a half-basis function is used at the end of the stripline and the coefficient of this basis function is the port current. Assuming that the vertical strip is electrically thin, we can assume that the current at the half-basis equals the vertical current (see Fig. 8). Thus, the half basis function is referred to as a "port basis." As denoted in (3), the interactions between port-basis (half-basis) and the regular-basis elements, which are represented by the $\mathbf{Z}^{ct}$ and $\mathbf{Z}^{tc}$ submatrices, are

$$
\begin{aligned}
Z_{ji}^{ct} &= j\omega \int_{y_j-(W_j/2)}^{y_j+(W_j/2)} \int_{x_j-L_j}^{x_j+L_j} \int_{y_i-(W_i/2)}^{y_i+(W_i/2)} \int_{x_i}^{x_i+L_i} \\
&\quad \cdot T_j^x(x) G_{A_{xx}}{}^{\text{int}}(x|x';\, y|y';\, 0|0) T_i^x(x')\, dx'\, dy'\, dx\, dy \\
&\quad - \frac{1}{j\omega} \int_{y_j-(W_j/2)}^{y_j+(W_j/2)} \int_{x_j-L_j}^{x_j+L_j} \int_{y_i-(W_i/2)}^{y_i+(W_i/2)} \int_{x_i}^{x_i+L_i} \\
&\quad \cdot \Pi_j^x(x) G_{\phi}^{\text{int}}(x|x';\, y|y';\, 0|0) \Pi_i^x(x')\, dx'\, dy'\, dx\, dy
\end{aligned} \tag{35}
$$

$$
\begin{aligned}
Z_{ji}^{tc} &= j\omega \int_{y_j-(W_j/2)}^{y_j+(W_j/2)} \int_{x_j}^{x_j+L_j} \int_{y_i-(W_i/2)}^{y_i+(W_i/2)} \int_{x_i-L_i}^{x_i+L_i} \\
&\quad \cdot T_j^x(x) G_{A_{xx}}{}^{\text{int}}(x|x';\, y|y';\, 0|0) T_i^x(x')\, dx'\, dy'\, dx\, dy \\
&\quad - \frac{1}{j\omega} \int_{y_j-(W_j/2)}^{y_j+(W_j/2)} \int_{x_j}^{x_j+L_j} \int_{y_i-(W_i/2)}^{y_i+(W_i/2)} \int_{x_i-L_i}^{x_i+L_i} \\
&\quad \cdot \Pi_j^x(x) G_{\phi}^{\text{int}}(x|x';\, y|y';\, 0|0) \Pi_i^x(x')\, dx'\, dy'\, dx\, dy.
\end{aligned} \tag{36}
$$

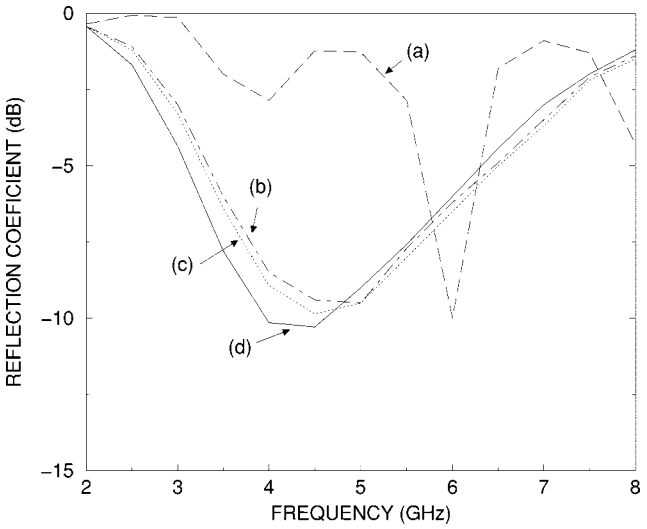

Fig. 11. Return loss of a single-slot antenna using: (a)Z_{DIFF}, (b) Z_{PORT} extracted using stub deembedding, and (c) Z_{PORT} after [23]. Referring to [6] $l_L = 50$ mm, $W_L = 2.5$ mm, $l_S = 30$ mm, $W_S = 2$ mm, $l_{\text{OFF}} = 10$ mm, $h = 1.57$ mm, and $\epsilon_r = 2.2$.

The transverse fields generated by the vertical current is described by elements

$$
\begin{aligned}
Z_{ji}^{xz} &= j\omega \int_{y_j-(W_j/2)}^{y_j+(W_j/2)} \int_{x_j-L_j}^{x_j+L_j} \int_{y_i-(W_i/2)}^{y_i+(W_i/2)} \int_{-h}^{0} \\
&\quad \cdot T_j^x(x) G_{A_{xz}}{}^{\text{int}}(x|x';\, y|y';\, 0|z')\, dz'\, dy'\, dx\, dy \\
&\quad - \frac{1}{j\omega} \int_{y_j-(W_j/2)}^{y_j+(W_j/2)} \int_{x_j-L_j}^{x_j+L_j} \int_{y_i-(W_i/2)}^{y_i+(W_i/2)} \int_{h}^{x_i+L_i} \\
&\quad \cdot \Pi_j^x(x) G_{\phi}^{\text{int}}(x|x';\, y|y';\, 0|z') \delta(z')\, dz'\, dy'\, dx\, dy.
\end{aligned} \tag{37}
$$

VII. Results

To illustrate the difference between the differential and circuit port characterizations, consider the strip coupled slot antenna in Fig. 6 with $l_L = 50$ mm, $W_L = 2.5$ mm, $l_S = 30$ mm, $W_S = 2$ mm, $l_{\text{OFF}} = 10$ mm, $h = 1.57$ mm, and $\epsilon_r = 2.2$. Details of the structure that is being used in developing the characterization is shown in Fig. 7, where the added open stub is 3-mm long. In Fig. 11, the reflection coefficient Γ_{DIFF} (corresponding to Z_{DIFF}) is compared to the reflection coefficient Γ_{PORT} (corresponding to Z_{PORT}) extracted using a stub deembedding method. The propagation constant and characteristic impedance were determined analytically. Not surprisingly, there is a significant discrepancy between the port and differential parameters. A problem with both stub deembedding methods is accounting for the fringing at the open-circuited stub. With both deembedding methods, the end of the stub was considered to be an open circuit. The error involved in this and the imprecision inherent in characterizing the transmission line (i.e., determining Z_c and γ) are responsible for the small discrepancy between the two procedures.

The central aim of this paper is to contrast the four differential characterization procedures. The quarter-wavelength stub

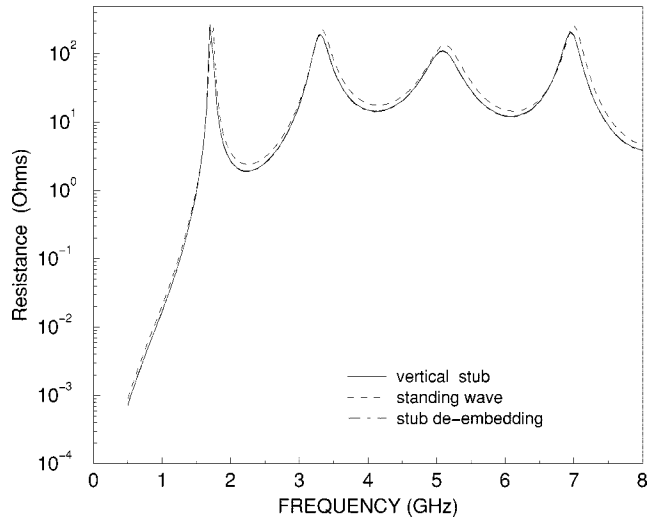

Fig. 12. Resistance of single-slot circuit.

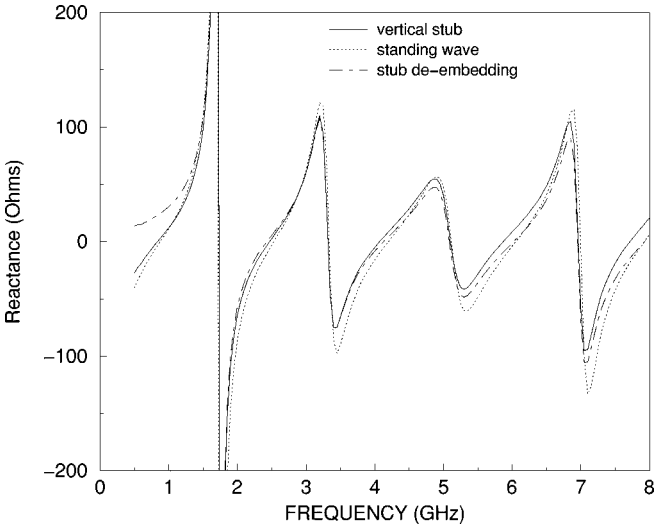

Fig. 13. Reactance of single-slot circuit.

deembedding procedure has already been contrasted above and will not be considered further as the long additional variable length of the stub is problematic. The real and imaginary components of $Z_{\rm PORT}$ for the stripline coupled slot antenna are presented in Figs. 12 and 13 using standing-wave characterization, stub deembedding, and vertical stub methods. The three methods yield consistent characterizations. The standing-wave and vertical stub methods yield almost identical resistive characterization (see Fig. 12). The three methods show larger variation when the port reactance is considered (see Fig. 12). This is attributed to energy storage (i.e., reactance) associated with the open stubs and the modification of the EM fields (again, a reactive effect) caused by the vertical stub. The inductive effect of the stub should be accounted for. In the paper, this is incorporated in the model of the active devices connected to the distributed network.

VIII. Discussion

This paper has dealt with the port definition required to interface circuit and EM analyses. The MoM EM analysis applied to structures with ground plane, with appropriately chosen current basis functions, yields network characterization at differential ports. In this paper, four techniques were constructed for transforming this characterization into the desired circuit port characterization. The techniques were all comparable and differ in terms of the additional structures required, affect on MoM matrix size, and ease of implementation. With all of these considerations, the vertical stub method is preferred, but it results in greater complexity in developing the Green's functions behind MoM analysis. Another contribution of this paper was the development of the MoM EM analysis for a three-layer SSS structure.

Appendix

A. Internal Region Green's Functions

The Green's functions of the region between the outer conductive layers (see Fig. 9) are described by G_d, a Dirichlet Green's function, and G_n, a Neumann Green's function, both of which are the solution of

$$(\nabla^2 + k^2)G_{d,\,n}(\mathbf{r},\,\mathbf{r}') = -\delta(\mathbf{r},\,\mathbf{r}') \tag{38}$$

and satisfy either Dirichlet or Neumann boundary conditions at the parallel plates. The boundary conditions of the potentials on the perfect conductor are

$$\phi = 0 \tag{39}$$
$$\frac{\partial \psi}{\partial n} = 0 \tag{40}$$
$$\hat{n} \times \mathbf{A} = 0 \tag{41}$$
$$\nabla_n \cdot \mathbf{A} = 0 \tag{42}$$
$$\hat{n} \times \nabla \times \mathbf{F} = 0 \tag{43}$$
$$\hat{n} \cdot \mathbf{F} = 0. \tag{44}$$

and the potential Green's functions for the internal region are then given by

$$G_{\phi}^{\rm int} = \frac{1}{\epsilon}\, G_d \tag{45}$$
$$G_{A_{xx}}^{\rm int} = \mu_0 G_d \tag{46}$$
$$G_{A_{yy}}^{\rm int} = \mu_0 G_d \tag{47}$$
$$G_{A_{xz}}^{\rm int} = \mu_0 G_n \tag{48}$$
$$G_{A_{yz}}^{\rm int} = \mu_0 G_n \tag{49}$$
$$G_{\psi}^{\rm int} = \frac{1}{\mu_0}\, G_n \tag{50}$$
$$G_{F_{xx}}^{\rm int} = -\epsilon G_n \tag{51}$$
$$G_{F_{yy}}^{\rm int} = -\epsilon G_n. \tag{52}$$

Using both modal and image representation, accelerated Green's function series are obtained [21]

$$G_d(\mathbf{r},\,\mathbf{r}') = g_d^{(m)} + \frac{1}{4\pi}\sum_{n=-\infty}^{\infty}\left(\frac{e^{-jkR_n^{+}}}{R_n^{+}} - \frac{e^{-jkP_n^{+}}}{P_n^{+}} - \frac{e^{-jkR_n^{-}}}{R_n^{-}} + \frac{e^{-jkP_n^{-}}}{P_n^{-}}\right) \tag{53}$$

$$G_n(\mathbf{r},\mathbf{r}') = g_n{}^{(m)} + \frac{1}{4\pi}\sum_{n=-\infty}^{\infty}\left(\frac{e^{-jkR_n{}^+}}{R_n{}^+} - \frac{e^{-jkP_n{}^+}}{P_n{}^+} + \frac{e^{-jkR_n{}^-}}{R_n{}^-} - \frac{e^{-jkP_n{}^-}}{P_n{}^-}\right) \quad (54)$$

where

$$g_d{}^{(m)}(\mathbf{r},\mathbf{r}') = \frac{1}{2\pi h}\sum_{n=1}^{\infty}\sin\left(\frac{n\pi}{2h}(z+h)\right) \times \sin\left(\frac{n\pi}{2h}(z'+h)\right)K_0(\alpha_n\rho_c) \quad (55)$$

and

$$g_n{}^{(m)}(\mathbf{r},\mathbf{r}') = -\frac{j}{8h}H_0{}^{(2)}(k\rho_c) + \frac{1}{2\pi h}\sum_{n=1}^{\infty} \quad (56)$$

$$\times\cos\left(\frac{n\pi}{2h}(z+h)\right)\times\cos\left(\frac{n\pi}{2h}(z'+h)\right) \cdot K_0(\alpha_n\rho_c). \quad (57)$$

The derivatives of the Green's functions with respect to the vertical axis z are

$$\frac{\partial G_d(\mathbf{r},\mathbf{r}')}{\partial z} = \frac{\partial g_d^{(m)}}{\partial z}(\mathbf{r},\mathbf{r}') + \frac{1}{4\pi}\sum_{n=-\infty}^{\infty} \times\left\{(z-z'-4nh)\times\left[e^{-jkP_n{}^+}\left(\frac{jk}{P_n^{+2}}+\frac{1}{P_n^{+3}}\right) - e^{-jkR_n{}^+}\left(\frac{jk}{R_n^{+2}}+\frac{1}{R_n^{+3}}\right)\right] + \left[z-z'-(2n+1)2h\right] \times\left[e^{-jkR_n{}^-}\left(\frac{jk}{R_n^{-2}}+\frac{1}{R_n^{-3}}\right) - e^{-jkP_n{}^-}\left(\frac{jk}{P_n^{-2}}+\frac{1}{P_n^{-3}}\right)\right]\right\} \quad (58)$$

$$\frac{\partial G_n(\mathbf{r},\mathbf{r}')}{\partial z} = \frac{\partial g_n^{(m)}}{\partial z}(\mathbf{r},\mathbf{r}') + \frac{1}{4\pi}\sum_{n=-\infty}^{\infty} \times\left\{(z-z'-4nh)\times\left[e^{-jkP_n{}^+}\left(\frac{jk}{P_n^{+2}}+\frac{1}{P_n^{+3}}\right) - e^{-jkR_n{}^+}\left(\frac{jk}{R_n^{+2}}+\frac{1}{R_n^{+3}}\right)\right] + \left[z-z'-(2n+1)2h\right] \times\left[e^{-jkP_n{}^-}\left(\frac{jk}{P_n^{-2}}+\frac{1}{P_n^{-3}}\right) - e^{-jkR_n{}^-}\left(\frac{jk}{R_n^{-2}}+\frac{1}{R_n^{-3}}\right)\right]\right\} \quad (59)$$

where

$$\frac{\partial g_d{}^{(m)}(\mathbf{r},\mathbf{r}')}{\partial z} = \frac{1}{4h^2}\sum_{n=1}^{\infty} n\cos\left(\frac{n\pi}{2h}(z+h)\right) \times\sin\left(\frac{n\pi}{2h}(z'+h)\right)K_0(\alpha_n\rho_c) \quad (60)$$

and

$$\frac{\partial g_n{}^{(m)}(\mathbf{r},\mathbf{r}')}{\partial z} = -\frac{1}{4h^2}\sum_{n=1}^{\infty} n\sin\left(\frac{n\pi}{2h}(z+h)\right) \times\cos\left(\frac{n\pi}{2h}(z'+h)\right)K_0(\alpha_n\rho_c). \quad (61)$$

Here,

$$\rho_0 = \sqrt{(x-x')^2+(y-y')^2} \quad (62)$$

$$\rho_c = \sqrt{\rho_0{}^2+c^2} \quad (63)$$

$$\alpha_n = \sqrt{\left(\frac{n\pi}{2h}\right)^2 - k^2} \quad (64)$$

$$R_n{}^+ = \sqrt{\rho_0{}^2+(z-z'-4nh)^2} \quad (65)$$

$$R_n{}^- = \sqrt{\rho_0{}^2+\left[z-z'-(2n+1)2h\right]^2} \quad (66)$$

$$P_n{}^+ = \sqrt{\rho_c{}^2+(z-z'-4nh)^2} \quad (67)$$

$$P_n{}^- = \sqrt{\rho_c{}^2+\left[z-z'-(2n+1)2h\right]^2} \quad (68)$$

K_0 is the modified Bessel function of order 0 and $c \geq 0$.

B. External Region Green's Functions

For the external region, the Green's function are the well-known solutions for half-space boundary conditions

$$G_\psi^{\text{ext}} = \frac{1}{4\pi\mu_0}\frac{e^{-jk_0r}}{r} \quad (69)$$

$$G_{F_{xx}}^{\text{ext}} = G_{F_{yy}}^{\text{ext}} = -\frac{\epsilon_0}{4\pi}\frac{e^{-jk_0}}{r}. \quad (70)$$

REFERENCES

[1] T. Itoh, *Numerical Techniques for Microwave and Millimeter-Wave Passive Structures*. New York: Wiley, 1989.

[2] L. P. Dunleavy and P. B. Katehi, "A generalized method for analyzing shielded thin microstrip discontinuities," *IEEE Trans. Microwave Theory Tech*, vol. 36, pp. 1758–1766, Dec. 1988.

[3] P. B. Katehi and N. Alexopoulos, "On the modeling of electromagnetically coupled microstrip antennas—The printed dipole," *IEEE Trans. Antennas Propagat.*, vol. AP-32, pp. 116–118, Dec. 1984.

[4] J. C. Rautio, "A new definition of characteristic impedance," in *IEEE MTT-S Int. Microwave Symp. Dig.*, June 1991, pp. 761–764.

[5] S. B. Goldberg, M. B. Steer, P. D. Franzon, and J. S. Kasten, "Experimental electrical characterization of interconnects and discontinuities in high speed digital systems," *IEEE Trans. Comp., Hybrids, Manufact. Technol.*, vol. 14, pp. 761–765, Dec. 1991.

[6] S. B. Goldberg, M. B. Steer, and P. D. Franzon, "Accurate experimental characterization of three-ports," in *IEEE MTT-S Int. Microwave Symp. Dig.*, June 1991, pp. 241–244.

[7] R. Gillard, J. H. Corre, M. Drissi, and J. Citerne, "A general treatment of matched terminations using integral equations modeling and application," *IEEE Trans. Microwave Theory Tech.*, vol. 42, pp. 2545–2553, Dec. 1994.

[8] E. K. L. Yeung, J. C. Beal, and Y. M. M. Antar, "Matched load simulation for multiport microstrip structures," *Electron. Lett.*, vol. 29, pp. 867–868, May 1993.

[9] C. E. Christoffersen and M. B. Steer, "Implementation of the local reference node concept for spatially distributed circuits," *Int. J. RF Microwave Computer-Aided Eng.*, vol. 9, no. 4, pp. 376–384, 1999.

[10] C. E. Christoffersen, M. A. Summers, and M. B. Steer, "Harmonic balance analysis for systems with circuit-field interaction," in *IEEE MTT-S Int. Microwave Symp. Dig.*, June 1998, pp. 1131–1134.

[11] T. W. Nuteson, G. P. Monahan, M. B. Steer, K. Naishadham, J. W. Mink, K. Kojucharoff, and J. Harvey, "Full-wave analysis of quasi-optical structures," *IEEE Trans. Microwave Theory Tech.*, vol. 44, pp. 701–710, May 1996.

[12] M. N. Abdulla, U. A. Mughal, and M. B. Steer, "Network characterization of a finite array of folded-slot antennas for spatial power combining application," in *Proc. IEEE AP-S Symp. Dig.*, July 1999, pp. 2370–2373.

[13] M. N. Abdulla, U. A. Mughal, H.-S. Tsai, M. B. Steer, and R. A. York, "A full-wave system simulation of a folded-slot spatial power combining amplifier array," in *IEEE MTT-S Int. Microwave Symp. Dig.*, June 1999, pp. 559–562.

[14] M. B. Steer, J. F. Harvey, J. W. Mink, M. N. Abdulla, C. E. Christoffersen, H. M. Gutierrez, P. L. Heron, C. W. Hicks, A. I. Khalil, U. A. Mughal, S. Nakazawa, T. W. Nuteson, J. Patwardhan, S. G. Skaggs, M. A. Summers, S. Wang, and A. B. Yakovlev, "Global modeling of spatially distributed millimeter-wave systems," *IEEE Trans. Microwave Theory Tech.*, vol. 47, pp. 830–839, June 1999.

[15] V. Eleftheriades and J. R. Mosig, "On the network characterization of planar passive circuits using the method of moments," *IEEE Trans. Microwave Theory Tech*, vol. 44, pp. 438–445, Mar. 1996.

[16] L. Zhu and K. Wu, "Characterization of unbounded multiport microstrip passive circuit using an explicit network-based method of moments," *IEEE Trans. Microwave Theory Tech.*, vol. 45, pp. 2114–2124, Dec. 1997.

[17] J. Hubert, J. Schoenberg, and Z. B. Popović, "High-power hybrid quasi-optical Ka-band amplifier design," in *IEEE MTT-S Int. Microwave Symp. Dig.*, vol. 2, June 1995, pp. 585–588.

[18] R. A. York and Z. B. Popović, *Active and Quasi-Optical Arrays for Solid-State Power Combining*. New York: Wiley, 1997.

[19] M. N. Abdulla and M. B. Steer, "A partitioning approach to large scale electromagnetic problems applied to an array of microstrip coupled slot antennas," in *IEEE MTT-S Int. Microwave Symp. Dig.*, June 1998, pp. 1783–1786.

[20] A. I. Khalil and M. B. Steer, "Circuit theory for spatially distributed microwave circuits," *IEEE Trans. Microwave Theory Tech.*, vol. 46, pp. 1500–1503, Oct. 1998.

[21] P. S. Simon, K. McInturff, D. L. Johnson, and J. A. Troychak, "Moment method analysis of a strip-fed finite slot using subdomain b asis function," in *IEEE Antenna Applicat. Symp. Dig.*, Sept. 1989, pp. 477–505.

[22] C. Chen and N. G. Alexopoulos, "Radiation by aperture antennas of arbitrary shape fed by a covered microstrip line," in *Proc. IEEE AP-S Symp. Dig.*, 1993, pp. 438–445.

[23] C. Chen, W. E. McKinzie, and N. G. Alexopoulos, "Strip-fed arbitrarily shaped printed-aperture antennas," *IEEE Trans. Antennas Propagat.*, vol. 45, pp. 1186–1198, July 1997.

[24] R. F. Harrington, *Field Computation by Moment Methods*. New York: Macmillan, 1968.

[25] M. N. Abdulla and M. B. Steer, "A finite double-layer slot array structure for spatial power combining amplifier," in *Proc. IEEE AP-S Symp. Dig.*, 1998, pp. 1206–1209.

Mostafa N. Abdulla (S'97–M'00) was born in Cairo, Egypt, in February 1970. He received the B.Sc. (with honors) and M.Sc. degrees from Ain Shams University, Cairo, Egypt, in 1992 and 1996, respectively, both in electronics and communication engineering, and the Ph.D. degree in electrical engineering from North Carolina State University, Raleigh, in 1999.

From 1992 to 1996, he was a Lecturer and Research Assistant in the Department of Electronics and Communication Engineering, Ain Shams University, where his research dealt with antennas and microwave circuits. From 1997 to 1999, he was with North Carolina State University, as a Research Assistant in the Electronics Research Laboratory, Department of Electrical and Computer Engineering, where he performed research in EM modeling of active antennas and spatial power-combining systems. In 1999, he was with Yazaki North America Inc., Canton, MI, as a Senior RF Engineer. Since 2000, he has been with the Intel Corporation, Sacramento, CA, as a Senior Engineer. His current interest include mixed-signal design methodology and RF circuit design.

Dr. Abdulla is a member of Phi Kappa Phi, the IEEE Antennas and Propagation Society (IEEE AP-S), and the IEEE Microwave Theory and Techniques Society (IEEE MTT-S).

Michael B. Steer (S'76–M'78–SM'90–F'99) received the B.E. and Ph.D. degrees in electrical engineering from the University of Queensland, Brisbane, Australia, in 1978 and 1983, respectively.

He is currently a Professor of electrical and computer engineering at North Carolina State University, Raleigh, NC. In 1999 and 2000, he was Professor in the School of Electronic and Electrical Engineering, The University of Leeds, where he still holds the Chair in Microwave and Millimeterwave Electronics. He was also Director of the Institute of Microwaves and Photonics, The University of Leeds. His research work has been closely tied to solving fundamental problems in modeling and implementing RF and microwave circuits and systems. His teaching and research interests are in global modeling of the physical layer of RF, microwave, and millimeter-wave electronic systems. His specific research is also directed at RF and microwave design, linearization of efficient power amplifiers, spatial power-combining systems, design of millimeter-wave and terahertz frequency communication and imaging systems, and high-efficiency low-cost RF technologies for wireless applications. He has organized many workshops and has taught many short courses on signal integrity, wireless, and RF design. He has authored or co-authored over 175 refereed papers and book chapters, including approximately 60 journal papers on topics related to RF, microwave, and high-speed digital design methodology. He has co-authored one book and holds one patent

Prof. Steer is active in the IEEE Microwave Theory and Techniques Society (IEEE MTT-S). In 1997, he was secretary of the Society and was an elected member of the Administrative Committee (AdCom) from 1998 to 2000.